

Spin-density-wave-induced anomalies in the optical conductivity of $A\text{Fe}_2\text{As}_2$, ($A=\text{Ca}, \text{Sr}, \text{Ba}$) single-crystalline iron pnictides

A. Charnukha,^{1,*} D. Pröpper,¹ T. I. Larkin,¹ D. L. Sun,¹ Z. W. Li,¹ C. T. Lin,¹ T. Wolf,² B. Keimer,¹ and A. V. Boris¹

¹Max-Planck-Institut für Festkörperforschung, Heisenbergstrasse 1, D-70569 Stuttgart, Germany

²Institut für Festkörperphysik, Karlsruhe Institute of Technology, D-76021 Karlsruhe, Germany

We report the complex dielectric function of high-quality $A\text{Fe}_2\text{As}_2$, ($A=\text{Ca}, \text{Sr}, \text{Ba}$) single crystals with $T_N \approx 150$ K, 200 K, and 138 K, respectively, determined by broadband spectroscopic ellipsometry at temperatures $10 \leq T \leq 300$ K and wavenumbers from 100 cm^{-1} to 52000 cm^{-1} . In CaFe_2As_2 we identify the optical spin-density-wave gap $2\Delta_{\text{SDW}} \approx 1250 \text{ cm}^{-1}$. The $2\Delta_{\text{SDW}}/(k_B T_N)$ ratio, characterizing the strength of the electron-electron coupling in the spin-density-wave state, amounts to ≈ 12 in CaFe_2As_2 , significantly larger than the corresponding values for the SrFe_2As_2 and BaFe_2As_2 compounds: 8.7 and 5.3, respectively. We further show that, similarly to the Ba-based compound, two characteristic SDW energy gaps can be identified in the infrared-conductivity spectra of both SrFe_2As_2 and CaFe_2As_2 and investigate their detailed temperature dependence in all three materials. This analysis reveals the existence of an anomaly in CaFe_2As_2 at a temperature $T^* \approx 80$ K, well below the Néel temperature of this compound, which implies weak coupling between the two SDW subsystems. The coupling between the two subsystems evolves to intermediate in the Sr-based and strong in the Ba-based material. The temperature dependence of the infrared phonons reveals clear anomalies at the corresponding Néel temperatures of the investigated compounds. In CaFe_2As_2 , the phonons exhibit signatures of SDW fluctuations above T_N and some evidence for anomalies at T^* . Investigation of all three materials in the visible spectral range reveals a spin-density-wave-induced suppression of two absorption bands systematically enhanced with decreasing atomic number of the intercalant. A dispersion analysis of the data in the entire spectral range clearly shows that CaFe_2As_2 is significantly more metallic than the other two compounds. Our results single out CaFe_2As_2 in the class of ThCr_2Si_2 -type iron-based materials by demonstrating the existence of two weakly coupled and extremely metallic electronic subsystems.

PACS numbers: 74.25.Gz, 74.70.Xa, 75.30.Fv, 78.30.Er

I. INTRODUCTION

In the family of iron-based superconductors,¹ the ThCr_2Si_2 -type materials are arguably the most widely studied.^{2,3} This fact owes to the early discovery^{4,5} and synthesis of large high-quality single-crystalline compounds of this class,⁶⁻⁹ thus allowing the entire arsenal of experimental condensed-matter techniques to be applied to them virtually simultaneously, giving rise to explosive progress in this area of research. The most attention of the community has since been focused on one particular member of the 122 class, BaFe_2As_2 . In this antiferromagnetic metal superconductivity can be induced by many different means such as electron or hole doping (e.g. by substituting cobalt for iron⁷ or potassium for barium,¹⁰ respectively), isoelectronic substitution (e.g. by substituting ruthenium for iron^{11,12} or phosphorus for arsenic¹³) or external pressure.² In all cases there emerges a phase diagram strikingly similar to that of the cuprate high-temperature superconductors,¹⁴ with superconductivity occurring in a dome-shaped region in the immediate vicinity of the antiferromagnetic phase. The development of a spin-density-wave order is accompanied by the opening of an energy gap in the excitation spectrum, which has been confirmed by numerous experimental techniques.² Investigations of the optical conductivity of this and other compounds have been instrumental in obtaining the value of the energy gap and characterising the energetics of the spin-density-wave order.¹⁵⁻¹⁸

Although the growth of CaFe_2As_2 (Ref. 19) and its phase diagram with respect to cobalt doping²⁰ were first reported

several years ago, the interest in this material started to build up upon the observation of its surprising sensitivity not only to doping and pressure but also to annealing.²¹ The direct observation of electronic nematicity due to anisotropic impurity scattering potential of substituted cobalt atoms in the underdoped region of the phase diagram of $\text{Ca}(\text{Fe}_{1-x}\text{Co}_x)_2\text{As}_2$ (Ref. 22,23), analogous to $\text{Ba}(\text{Fe}_{1-x}\text{Co}_x)_2\text{As}_2$ (Refs. 24-27), has brought CaFe_2As_2 to the forefront of condensed-matter research. Notwithstanding all this interest and some preliminary measurements²⁸ (normal-state optical-conductivity data from Ref. 28 were also reproduced in Ref. 16), as well as extensive studies of the charge dynamics in both the parent ($\text{Ba}, \text{Sr}, \text{Eu}$) Fe_2As_2 (Refs. 15,16,29-32) and most of their doped/substituted superconducting derivatives,^{17,33-45} the detailed investigation of the charge dynamics in CaFe_2As_2 and a systematic comparison with other 122-type materials are still lacking.

In the present work we fill this gap by reporting broad band ellipsometric study of not only CaFe_2As_2 but also its Sr- and Ba-based counterparts and a systematic comparison thereof over a wide spectral range, complemented by a thorough Drude-Lorentz analysis of the interband and itinerant optical response. We find that, similarly to the previous reports on BaFe_2As_2 and SrFe_2As_2 (Ref. 15,40), two distinct spin-density-wave energy gaps can be identified in the Ca-based compound. In order to address the degree of interplay between these two spin-density-wave subsystems we further carried out a detailed temperature-dependent study of the far-infrared conductivity of all these compounds and discovered the presence of an anomaly at $T^* \approx 80$ K in CaFe_2As_2 well

below its Néel temperature at the frequencies of the smaller spin-density-wave energy gap. This observation clearly indicates that the two electronic subsystems in this material are weakly coupled (as shown for the analogous case of superconductivity in Refs. 46–50). Further comparison with the Sr- and Ba-based counterparts reveals that this coupling evolves via intermediate in the former to strong in the latter compound, systematically with increasing atomic number of the intercalant. The temperature dependence of the infrared phonons shows a clear anomaly at T_N in all three compounds, whereby the spin-density-wave-induced modifications of the phonon properties set in exactly at T_N in both Ba- and Sr-based materials but at somewhat higher temperatures in CaFe_2As_2 , suggesting the early development of spin-density-wave fluctuations and their impact on the lattice. We also find a possible indication of T^* in the temperature dependence of the Ca-related phonon intensity $\Delta\varepsilon_0$.

Investigation of the optical conductivity in the visible spectral range further reveals the existence of a spin-density-wave-induced suppression of two absorption bands, previously reported for SrFe_2As_2 in Ref. 51, also in the Ca- and Ba-based compounds, with the intensity of the suppression systematically enhanced with decreasing atomic number of the intercalating atom.

Finally, a thorough dispersion analysis reveals a dramatic enhancement of metallicity with decreasing atomic number of the intercalant manifested in the growing total plasma frequency and a systematic evolution of a number of other electronic parameters.

II. EXPERIMENTAL DETAILS

The parent $(\text{Ca,Sr})\text{Fe}_2\text{As}_2$ single crystals were grown in zirconia crucibles sealed in quartz ampoules under argon atmosphere.⁵² From dc resistivity and magnetization measurements we obtained the Néel temperatures $T_N = 150$ and 200 K for CaFe_2As_2 (see Fig. 1) and SrFe_2As_2 (Ref. 52), respectively. BaFe_2As_2 single crystals were grown from As-rich self-flux in a glassy carbon crucible using prereacted FeAs_2 powders mixed with Ba and As.⁹ The sample surface was cleaved prior to every optical measurement. The full complex optical conductivity $\sigma(\omega)$ was obtained in the

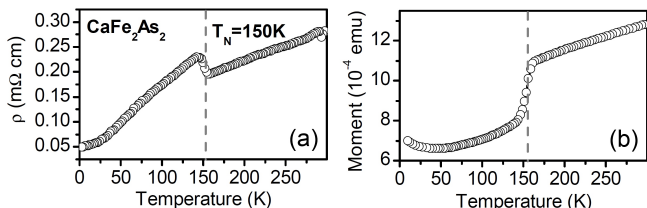


FIG. 1: Temperature dependence of the resistivity (a) and magnetic moment (b) of the CaFe_2As_2 single crystals used in the present study. Both measurements reveal a clear signature of a spin-density-wave transition at about 150 K and the absence of any secondary phase transitions at lower temperatures.

range $100 - 52000 \text{ cm}^{-1}$ using broad band ellipsometry, as described in Ref. 53. The measurements in the lowest far-infrared spectral range were carried out at the infrared beamline of the ANKA synchrotron light source at Karlsruhe Institute of Technology, Germany.

III. RESULTS AND DISCUSSION

A. Optical conductivity of $A\text{Fe}_2\text{As}_2$, ($A=\text{Ca, Sr, Ba}$)

The independently obtained real and imaginary parts of the complex optical conductivity $\sigma(\omega) = \sigma_1(\omega) + i\sigma_2(\omega)$ of the $A\text{Fe}_2\text{As}_2$, ($A=\text{Ca, Sr, Ba}$) compounds in the entire investigated spectral range at several representative temperatures is shown in Fig. 2. The far-infrared response of CaFe_2As_2 [Fig. 2(a) and 2(d)] in the normal state is dominated by a strong itinerant response, clearly manifested in the large positive values of both $\sigma_1(\omega)$ and $\sigma_2(\omega)$. Below the spin-density-wave transition temperature of 150 K this itinerant response experiences a dramatic suppression due to the opening of an energy gap in the quasiparticle excitation spectrum, as previously observed in this and other 122-type iron-based materials.^{15–18} Due to the conservation of the total number of electrons, the missing area under the conductivity curve at low frequencies is transferred to higher energies, which results in a formation of a “hump” structure.^{54,55} In the most common case when the spin-density-wave energy gap does not cover the entire Fermi surface of a material and, therefore, the optical conductivity remains non-zero at all frequencies, determination of the optical quasiparticle excitation gap 2Δ from the conductivity spectra is difficult but it can be approximated by the energy, at which the low-temperature conductivity spectrum crosses the one at the Néel temperature for the first time.⁵⁵ This energy $2\Delta_L^{\text{SDW}}$ is marked by the right vertical dashed lines in panel 2(a). At lowest frequencies, the optical conductivity of CaFe_2As_2 reveals a change in its shape at 10 K as compared to intermediate temperatures below T_N , which indicates the presence of another spin-density-wave gap, with a smaller magnitude $2\Delta_S^{\text{SDW}}$ [left vertical dashed line in panel 2(a)]. This observation is analogous to the previous report of two different spin-density-wave energy gaps in the Sr- and Ba-based compound of the same class.^{15,29,40} Our own ellipsometric measurements on the Sr- and Ba-based compounds, shown in Fig. 2(b), 2(e) and 2(c), 2(f), fully reproduce and confirm previously reported data,^{15–18,29,31,40} provide additional information due to the independently obtained real and imaginary parts of the optical conductivity, and allow for a systematic investigation of the electronic properties of the ThCr_2Si_2 -type iron-based materials as a function of the intercalating atom.

First of all, we find that, although the Néel temperature does not show a systematic dependence on the atomic number of the intercalating atom, the gap ratios, which quantify the strength of the coupling to a boson mediating a given electronic instability, certainly do display some systematic trends, as shown in Table I. Here we define the gap ratio of an itinerant antiferromagnetic material with an optical spin-density-

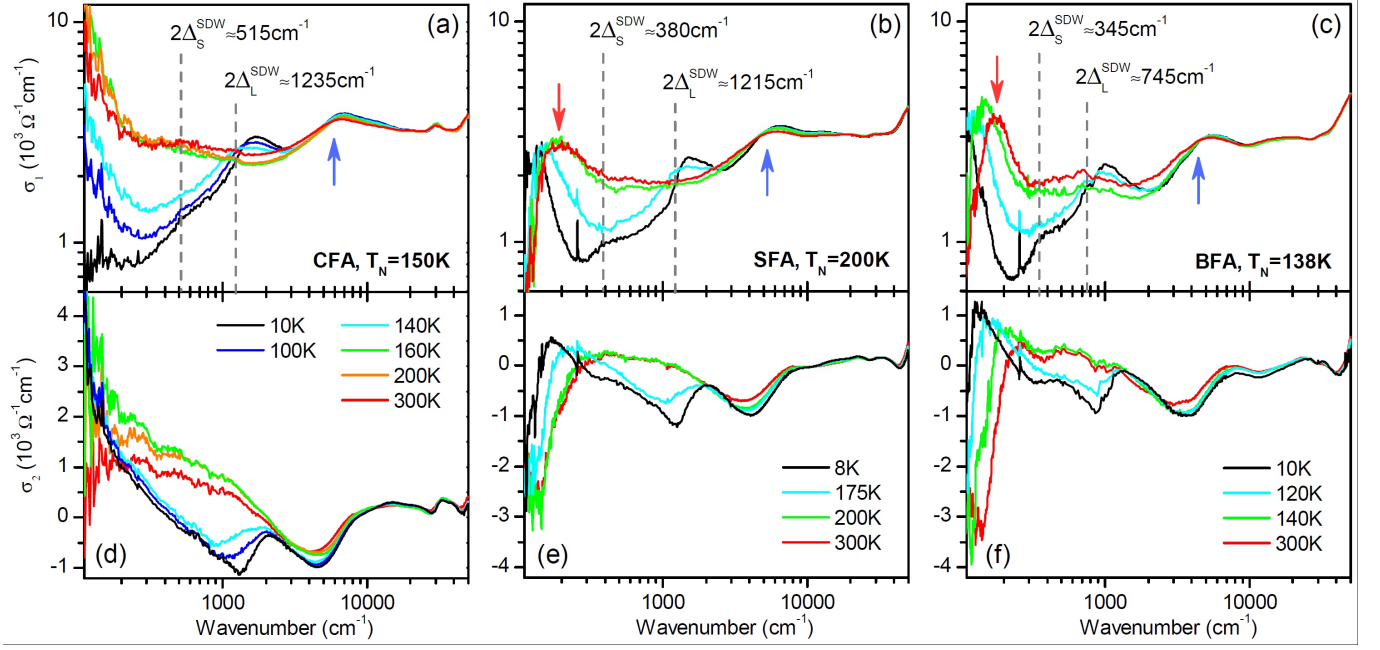


FIG. 2: (a)–(c) Real part of the complex optical conductivity of CaFe_2As_2 (a), SrFe_2As_2 (b), and BaFe_2As_2 (c). Characteristic energies of the large and small optical spin-density–wave gaps ($2\Delta_{L,S}^{\text{SDW}}$, vertical dashed lines) are defined as the intersection points between the lowest and the Néel temperatures for the large gap and the deviation point for the small gap (see text). Strongly temperature dependent absorption bands are marked with blue arrows. Low-energy peak feature observed in Sr- and Ba-based compounds but not in CaFe_2As_2 is indicated with red arrows. (d)–(f) The corresponding imaginary part of the complex optical conductivity.

wave energy gap 2Δ and a Néel temperature T_N as $2\Delta/k_B T_N$, where k_B is the Boltzmann constant. The values of the large and small optical spin-density–wave gaps are extracted from the experimentally obtained optical conductivity as described above and indicated in Fig. 2 with vertical dashed lines.

Table I shows that, albeit the Ca-based compound has a Néel temperature significantly lower than that of the Sr-based counterpart and comparable to that of BaFe_2As_2 , its both gap ratios are significantly larger than those of the other two materials, which implies a much stronger electronic instability in this compound. In addition, the larger gap ratio $2\Delta_L^{\text{SDW}}/k_B T_N$ gradually decreases with the increasing atomic number of the intercalant.

The far-infrared optical conductivity of SrFe_2As_2 and

BaFe_2As_2 at lowest frequencies is dominated by a peak feature [red arrows in Figs. 2(b),2(c)] reminiscent of the collective excitation previously observed in the nearly optimally doped high-temperature cuprate superconductor $\text{YBa}_2\text{Cu}_3\text{O}_{6+x}$ pristine⁵⁶ and after irradiation with helium ions.⁵⁷ A similar albeit weaker feature has also been identified in the far-infrared optical response of superconducting $\text{Ba}(\text{Fe}_{0.92}\text{Co}_{0.08})_2\text{As}_2$ in Ref. 58. One of the possible origins of this feature is charge-carrier localization, as observed in disordered doped superconductors.^{59–61}

At higher energies the optical conductivity of all three compounds shows a strongly temperature-dependent absorption band centered at about 5000–6000 cm^{-1} , as well as at UV energies in the case of BaFe_2As_2 , as shown in Figs. 2(a)–2(c) with blue arrows.

TABLE I: Large and small optical spin-density–wave gap $2\Delta_{L,S}^{\text{SDW}}$ as inferred from the optical conductivity spectra in Fig. 2 and the corresponding gap ratios.

	CaFe_2As_2	SrFe_2As_2	BaFe_2As_2
$2\Delta_L^{\text{SDW}}, \text{cm}^{-1}$	1235	1215	745
$2\Delta_S^{\text{SDW}}, \text{cm}^{-1}$	515	380	345
$k_B T_N, \text{cm}^{-1}$	105	140	97
$2\Delta_L^{\text{SDW}}/k_B T_N$	11.8	8.7	7.7
$2\Delta_S^{\text{SDW}}/k_B T_N$	4.9	2.7	3.6
$2\Delta_L^{\text{SDW}}/2\Delta_S^{\text{SDW}}$	2.4	3.2	2.14

B. Temperature dependence of the SDW-induced suppression

The existence of two separate spin-density–wave energy gaps raises a question as to the degree of interaction between the corresponding electronic subsystems. This question becomes particularly difficult to address in the presence of as many Fermi-surface sheets as is the case for the iron-based materials, which often commonly possess five separate Fermi-surface sheets in the first Brillouin zone. This complexity arises mainly due to the fact that the optical conductivity represents an intertwined response of all electronic subsystems at once. To shed some light onto this issue, in addition to our

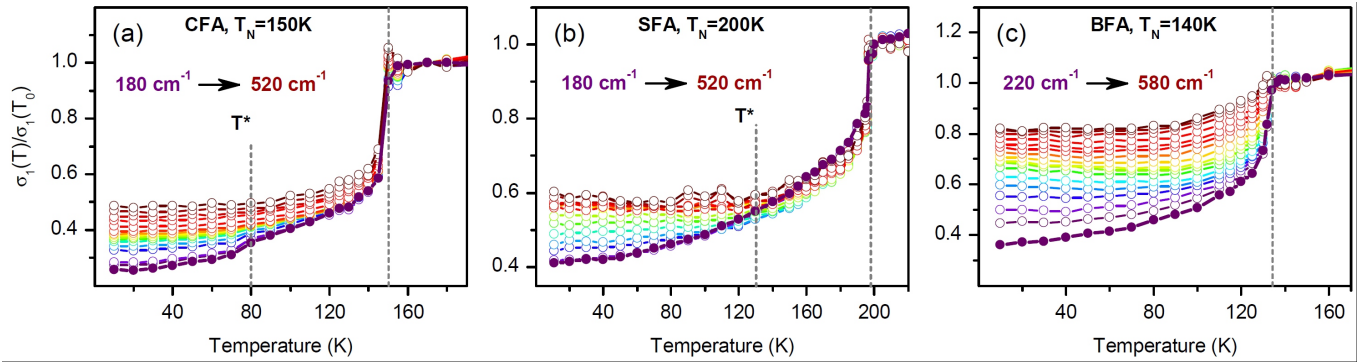


FIG. 3: (a)–(c) Detailed temperature dependence of the real part of the complex optical conductivity of CaFe_2As_2 (a), SrFe_2As_2 (b), and BaFe_2As_2 (c) on a fine grid of wavenumbers in the far-infrared spectral range, normalized to the value of the optical conductivity at $T = T_0$ close to T_N ($T_0 = 170$ K, 200 K, and 140 K for the Ca-, Sr-, and Ba-based compounds, respectively). The grid of wavenumbers runs from 180 cm^{-1} (blue colors) to 520 cm^{-1} (red colors) in steps of 20 cm^{-1} with the exception of the spectral window of the 260 cm^{-1} phonon. Spin-density-wave-related features in the temperature dependence of the optical conductivity (vertical dashed lines), for interpretation see text. The lowest-frequency temperature dependence is plotted as filled circles unlike the rest (open circles) to emphasize the change in the temperature dependence of the optical conductivity.

broad band ellipsometric measurements at several representative temperatures, we have carried out detailed measurements in the far-infrared spectral range (i.e. in the range where the real part of the optical conductivity experiences a drastic suppression, as shown in Fig. 2) with a very fine temperature grid for all three materials in question. The results are compiled in Fig. 3, which shows the temperature dependence of the optical conductivity normalized to its value at $T = T_0$ close to T_N ($T_0 = 170$ K, 200 K, and 140 K for the Ca-, Sr-, and Ba-based compounds, respectively) at an equidistant set of wavenumbers from 180 cm^{-1} (blue colors) to 520 cm^{-1} (red colors) in steps of 20 cm^{-1} with the exception of the spectral window of the 260 cm^{-1} phonon.

The temperature dependence of the normalized conductivity shows a very pronounced drop for all compounds at their respective Néel temperatures (right vertical dashed lines) due to the onset of spin-density-wave order, with a clear mean-field order-parameter-like temperature dependence at large wavenumbers (red colors). This temperature dependence changes, however, as one moves toward progressively smaller wavenumbers and in the case of CaFe_2As_2 reveals a clear second suppression feature at a temperature T^* of about 80 K. This second feature becomes washed out in the Sr-based compound, although the temperature dependence of σ_1 at smallest wavenumbers remains markedly different from that at large wavenumbers and some sort of an analogue of T^* can be sketched also in this case, although there is no clear second suppression feature present in any of the separate temperature dependences themselves. Finally, in the case of BaFe_2As_2 , the change in the temperature dependence of σ_1 between large and small wavenumbers becomes hardly noticeable, with minute changes below ≈ 60 K.

The presence of a second suppression feature in the temperature dependence of the real part of the optical conductivity at small enough wavenumbers in CaFe_2As_2 indicates, that the electronic subsystem that develops the smaller spin-density-wave energy gap $2\Delta_S^{\text{SDW}}$ preserves some knowledge about

its own Néel temperature that it *would have* if this subsystem were completely independent from the other(s). In any real material all electronic subsystems are coupled, even if weakly, so that all spin-density-wave energy gaps open at the same T_N . However, in case of weak intersubsystem coupling, those with smaller gaps exhibit an anomaly below the real Néel temperature, as is the case in CaFe_2As_2 . Such an effect has been predicted theoretically for the analogous case of multiband superconductivity^{46,47} and discovered experimentally in FeSe_{1-x} in Refs. 48–50. This argument thus suggests that in the Ca-based material the two electronic subsystems developing the large and the small spin-density-wave energy gap are weakly coupled. Naturally, as the coupling between such electronic subsystems increases, the temperature dependence of the small gap would gradually approach that of the large gap via an intermediate state when it already does not show any anomaly but still has not matched the temperature dependence of the large gap. Figure 3(b) provides evidence for such a behavior in the Sr-based iron pnictide. Finally, the temperature dependence of the normalized optical conductivity in BaFe_2As_2 is almost the same at all wavenumbers, both in the region of the large spin-density-wave gap and in that of the small one, indicating strongly coupled electronic subsystems in this compound. Thus, by monitoring the detailed temperature dependence of the optical conductivity in the far-infrared spectral range on a fine grid of wavenumbers, a gradual transition could be observed from weak coupling between the electronic subsystems developing the two different spin-density-wave energy gaps in CaFe_2As_2 , via intermediate coupling in SrFe_2As_2 , to strong coupling between them in BaFe_2As_2 , systematically with increasing atomic number of the intercalant.

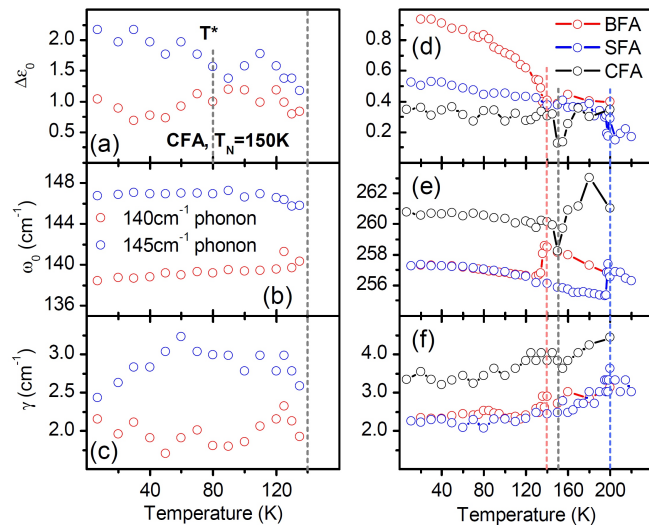


FIG. 4: (a)–(c) Temperature dependence of the strength $\Delta\varepsilon$, position ω_0 , and the width γ of the Ca-related phonon below the Néel transition temperature of CaFe_2As_2 , split due to the lowering of the crystallographic symmetry from tetragonal to orthorhombic at the concomitant structural transition (right vertical dashed line). The temperature T^* of the small optical spin-density-wave gap $2\Delta_S^{\text{SDW}}$ [left vertical dashed line in (a)] as inferred from Fig. 3(a). (d)–(f) Temperature dependence of the strength $\Delta\varepsilon$, position ω_0 , and the width γ of the phonon due to the vibrations of Fe and As ions. Vertical dashed lines indicate the Néel transition temperatures of the Ca-, Sr-, and Ba-based compounds (grey, light blue, pink, respectively).

C. Temperature dependence of the far-infrared phonons

We now use the same detailed ellipsometric measurements of the real and imaginary parts of the optical conductivity to analyze and compare between the three different compounds the temperature dependence of the strength, position, and the width of the far-infrared optical phonons. As can be seen in Fig. 2, the low-energy phonon due to the vibrations of the intercalating ions can be seen at $\approx 140 \text{ cm}^{-1}$ in the Ca-based compound but not in the Sr- and Ba-based counterparts due to the much smaller mass of the former, which pushes this phonon into the accessible experimental spectral range. The phonon arising from vibrations of Fe and As is seen at an approximately the same position of 260 cm^{-1} in all three materials. The detailed temperature dependence of the Lorentz parameters of the Ca-related phonon at temperatures below T_N , where it can be clearly resolved, as well as the comparison of the Lorentz parameters of the 260 cm^{-1} -phonon in all three compounds is shown in Fig. 4.

In the CaFe_2As_2 compound, the splitting of the Ca-related phonon at the magnetostructural transition can be clearly resolved, similarly to the previously reported splitting of the Ba-related phonon in the sister compound,³¹ and amounts to about 8 cm^{-1} [Fig. 4(b)]. Within the noise floor the temperature dependence of the width of these two phonons, plotted in Fig. 4(c), does not appear to display any anomalies. That of the phonon strength $\Delta\varepsilon$, on the other hand, seems to slightly change at the temperature T^* [left vertical dashed line in (a)]

inferred from Fig. 3(a), albeit this change is quite close to the limit of the fit uncertainty.

The temperature dependence of all Lorentz parameters of the Fe-As phonon in all three compounds, Fig. 4(d)–(f), shows noticeable anomalies at the respective Néel temperatures (grey, light blue, and pink vertical dashed lines for Ca-, Sr-, and Ba-based compounds, respectively). In SrFe_2As_2 and BaFe_2As_2 the phonon intensity $\Delta\varepsilon$ and position ω_0 change abruptly at the magnetostructural transition temperature, as shown in Fig. 4(d), 4(e), whereas in CaFe_2As_2 , quite surprisingly, the spin-density-wave-induced changes seem to set in already at somewhat higher temperatures [Fig. 4(e)]. This observation indicates the existence of incipient critical lattice strain at temperatures higher than the magnetostructural transition temperature in this compound, which may be related to the electronic nematicity recently discovered in a doped compound of this class.²³ In addition, while the width and the position of the Fe-As phonon in both Sr- and Ba-doped compounds [Fig. 4(e), 4(f)] display essentially identical magnitude and behavior, those of the Ca-doped material are significantly larger. While the somewhat broader phonon feature could, in principle, be traced back to the quality of the sample surface or the sample itself, the harder Fe-As phonon of Ca-based compound compared to its Sr- and Ba-based counterparts must be intrinsic. Such a hardening most likely results from the shorter Ca-As and Fe-As bond lengths compared to those in the Sr- and Ba-based compounds and has also been observed in inelastic-neutron-scattering measurements on CaFe_2As_2 , BaFe_2As_2 and predicted by ab-initio calculations⁶².

D. Spin-density-wave-induced anomaly in the visible

Having investigated the spin-density-wave-induced anomalies in the infrared spectral range, let us turn to the charge dynamics in the 122 compounds at visible frequencies.⁶⁵ Recently, a criticality-induced suppression of an absorption band at energies, much higher than the corresponding energy gaps, has been reported in both the optimally doped superconducting $\text{Ba}_{0.68}\text{K}_{0.32}\text{Fe}_2\text{As}_2$ and the antiferromagnetic SrFe_2As_2 (Ref. 51). The analysis of the spectral-weight transfer across the spin-density-wave transition carried out in the same work, revealed that high energies up to 4 eV are involved in the spectral-weight redistribution and that the f -sum rule is fully satisfied above the suppressed absorption band in the visible spectral range. It appears to be of interest whether in other parent compounds of the same 122-type the spin-density-wave energetics is similar or rather shows a systematic variation with the atomic number of the intercalant within the class. To this end we have carried out accurate ellipsometric measurements in the visible spectral range to match the data quality of Ref. 51 and compare the intensity and location of the spin-density-wave-suppressed absorption bands, as well as the spectral-weight redistribution in the entire investigated spectral range, in all three parent compounds.

The results are presented in Fig. 5. Panels 5(a)–(c) show

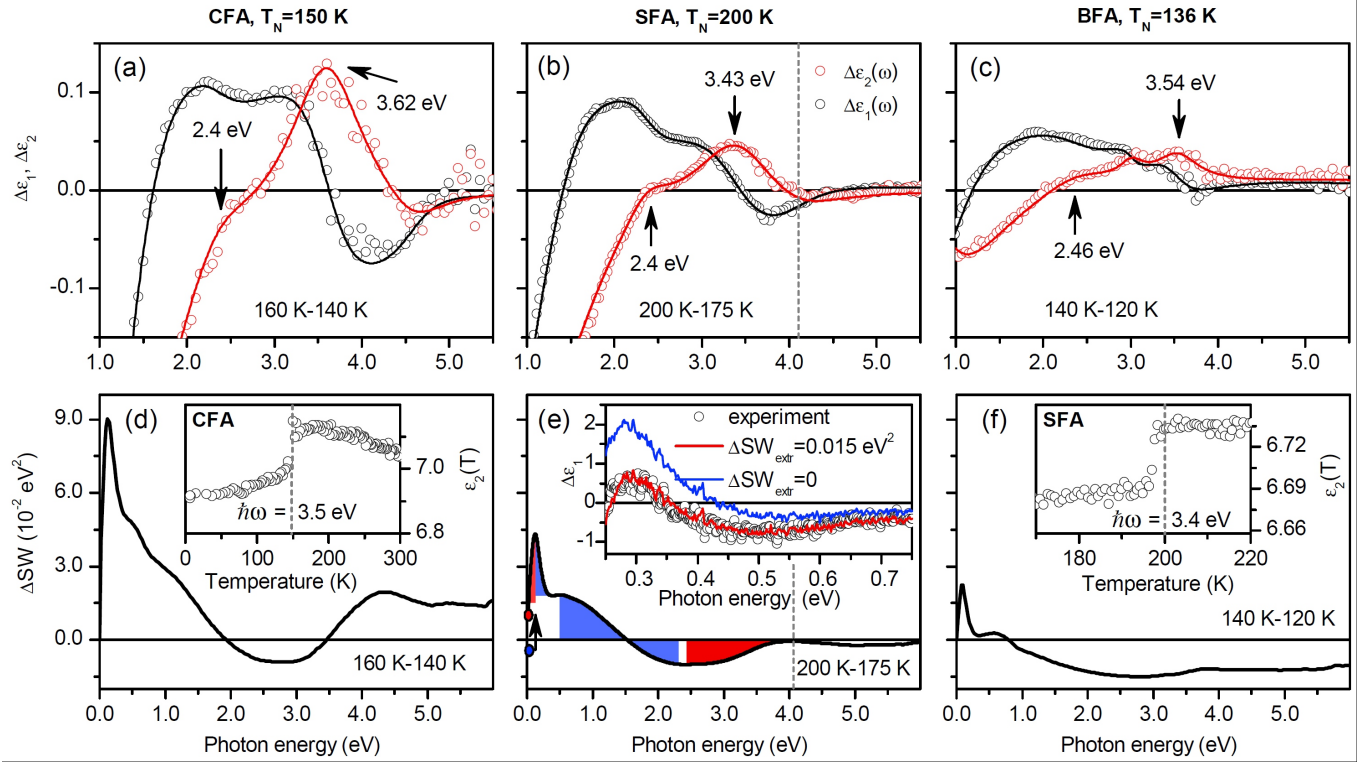


FIG. 5: (a)–(c) Difference real and imaginary parts of the dielectric function $\Delta\epsilon_1$, $\Delta\epsilon_2$ in the visible spectral range between the temperatures above and below the Néel transition temperature, as specified in the panels. The arrows indicate the two spin-density-wave-suppressed absorption bands. (d)–(f) Spectral-weight redistribution between the same temperatures and in the same compounds as in (a)–(c) as a function of photon energy. Blue and red areas in (e) indicate the regions of spectral-weight gain and loss, respectively, in the magnetic versus the normal state. [Inset in (e)], Real part of the dielectric function and the Kramers-Kronig transformations of the real part of the optical conductivity of SrFe₂As₂ with different amount of spectral weight contained in the extrapolation region at low frequencies (solid lines, colors match filled circles). [Insets in (d),(f)] Temperature scan of ϵ_2 in CaFe₂As₂ at 3.5 eV and in SrFe₂As₂ at 3.4 eV, respectively. Panel (e), the inset therein, as well as in (f) adapted by permission from Macmillan Publishers Ltd: Nature Communications Ref. 51, copyright (2011).

the difference real and imaginary parts of the dielectric function $\epsilon(\omega) = 1 + 4\pi i\sigma(\omega)/\omega$ in the visible spectral range. The difference is taken between the temperatures above and below the material's Néel transition temperature: 160 K and 140 K, 200 K and 175 K, and 140 K and 120 K for CaFe₂As₂, SrFe₂As₂, and BaFe₂As₂, respectively. These spectra reveal a clear suppression of absorption at optical frequencies. The magnetostructurally induced character of this suppression is confirmed by drastic drop in the temperature dependence of the imaginary part of the dielectric function ϵ_2 at the Néel temperature, shown in the inset of Figs. 5(d), 5(f) for the Ca- and Sr-based compounds, respectively. The suppressed optical response of all three iron pnictides shown in Figs. 5(a)–(c) reveals the contribution of two absorption bands and the systematic evolution of their suppression intensities with the atomic number: the suppression of both bands reduces upon going from lighter to heavier intercalating atoms.

We now move to the analysis of the spectral-weight redistribution across the spin-density-wave transition presented in Figs. 5(d), 5(e), and 5(f) for the case of Ca-, Sr-, and Ba-based material, respectively. The energy-dependent spectral weight is defined as the integral of the real part of the optical

conductivity $\sigma_1(\omega)$ up to a certain cut-off frequency Ω :

$$SW(\Omega) = \int_0^{\Omega} \sigma_1(\omega) d\omega.$$

Several common features can be identified in the energetics of the spin-density-wave transition: the spectral weight from below the optical spin-density-wave gap $2\Delta^{\text{SDW}}$ [lowest-energy red area in Fig. 5(e) and the corresponding areas in Figs. 5(d),(f)] is redistributed to energies directly above the optical gap [subsequent blue area in Fig. 5(e) and the corresponding areas in Figs. 5(d),(f)]. However, the spectral weight gained directly above the optical gap does not balance that lost within the gap, which implies that higher-energy processes beyond the characteristic magnetic energy scales proposed for these materials are affected by the spin-density-wave transition, including the spin-density-wave-suppressed band in the visible spectral range [higher-energy blue and red areas in Fig. 5(e) and the corresponding areas in Figs. 5(d),(f)]. Such a high-energy modification of the spectral weight might originate in a redistribution of the electronic population between several bands at the spin-density-wave transition, as suggested for SrFe₂As₂ in Ref. 51.

These commonalities notwithstanding, it is clear from

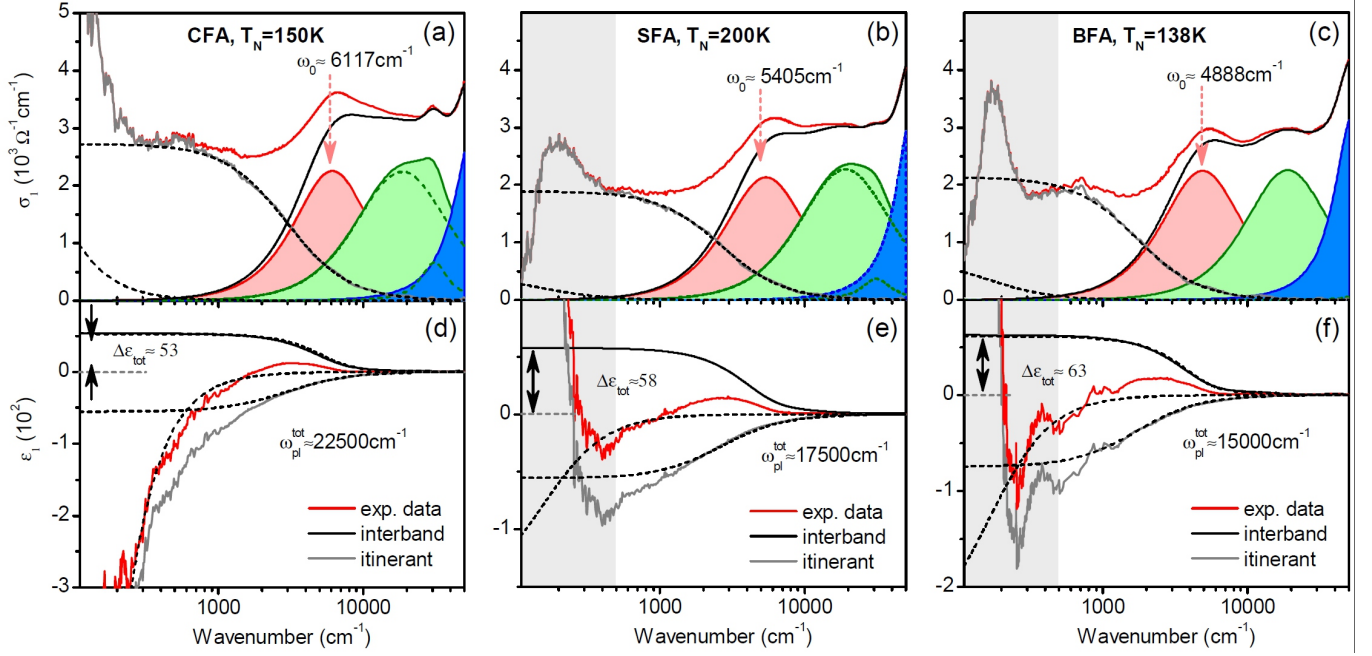


FIG. 6: Real part of the optical conductivity (a)–(c) and dielectric function (d)–(f) of the Ca-, Sr-, and Ba-based compounds at 300 K (red line) and the corresponding interband [red, green, and blue areas in (a)–(c)] and itinerant (grey line) contributions obtained in a Drude-Lorentz dispersion analysis as described in the text. The partial Drude contributions are shown as black dashed lines. The lowest clearly identifiable absorption band is indicated with a pink arrow. Major partial Lorentz contributions to the absorption band in the visible (green area) are plotted as green dashed lines in (a)–(c). The total contribution of all interband transitions (black line). The grey-shaded area in (b), (c) and (e), (f) indicates the spectral range excluded from the Drude-Lorentz fit due to the presence of a low-energy collective excitation.

Figs. 5(d)–(f) that the overall intensity of the spectral-weight redistribution at the spin-density–wave transition decreases systematically with increasing atomic number of the intercalant even though the corresponding Néel temperatures do not reflect this behavior (T_N is almost the same in the Ca- and Ba-based compound, whereas the amplitude of the spectral-weight redistribution is more than three times larger).

E. Itinerant properties

Systematic trends similar to those found in the overall energetics of the 122 parent compounds investigated in this work can also be identified in the itinerant-charge-carrier response. However, whereas the former could be revealed already in the raw ellipsometric data, the extraction of the properties of the latter requires careful elimination of the interband contribution to the optical conductivity by means of a dispersion analysis (e.g. as carried out in Ref. 63), which allows one to isolate the inherent itinerant response. In the present work we have analyzed the free-charge-carrier and interband contributions in the standard Drude-Lorentz model.

In this method, the optical conductivity $\sigma(\omega) = \sigma_1(\omega) + i\sigma_2(\omega)$ or, equivalently, the full complex dielectric function $\varepsilon(\omega) = 1 + 4\pi i\sigma(\omega)/\omega$ (in CGS units) is fitted with an ex-

pression of the following form:

$$\varepsilon(\omega) = - \sum \frac{\omega_{pl,j}^2}{\omega^2 + i\gamma_j\omega} + \sum \frac{\Delta\varepsilon_j\omega_{0j}^2}{(\omega_{0j}^2 - \omega^2) - i\Gamma_j\omega}, \quad (1)$$

where the first sum runs over all Drude and the second one over all Lorentz terms. $\omega_{pl,j}$ and γ_j are the plasma frequency and the quasiparticle scattering rate of the partial itinerant response and $\Delta\varepsilon_j$, ω_{0j} , Γ_j are the static permittivity contribution, the center frequency and the width of the Lorentzian oscillators used to model the interband transitions, respectively. The function in Eq. 1 is fitted simultaneously to the real and imaginary parts of the dielectric function.

The oscillator parameters obtained in such a fit for all three 122 parent compounds are summarized in Table II. The contribution of the most important interband transitions to the real part of the optical conductivity is broken down in Figs. 6(a)–6(c) (red, green, and blue shaded areas) for the Ca-, Sr-, and Ba-based compounds, respectively, and their integral contribution to the real part of both the optical conductivity [black lines in Figs. 6(a)–6(c)] and the dielectric function [black lines in Figs. 6(d)–6(f)], as well as the extracted itinerant response (grey lines in all panels), is also shown. The overall structure of the interband transitions is very similar in all three compounds. The lowest clearly identifiable interband transition, previously found to be strongly renormalized with respect to the prediction of band-structure calculations and to give an unusually large contribution to the total zero-frequency interband permittivity $\Delta\varepsilon_{tot}$ of the order of 60 in the optically

TABLE II: Parameters of the Drude and Lorentzian terms in (1) obtained from the dispersion analysis of the optical conductivity of CaFe_2As_2 , SrFe_2As_2 , and BaFe_2As_2 at room and Néel temperature (shown for room temperature in Fig. 6).

j	CaFe_2As_2			SrFe_2As_2			BaFe_2As_2		
	$\Delta\varepsilon_j$	$\omega_{0j} (\omega_{\text{pl},j}), \text{cm}^{-1}$	$\Gamma_j (\gamma_j), \text{cm}^{-1}$	$\Delta\varepsilon_j$	$\omega_{0j} (\omega_{\text{pl},j}), \text{cm}^{-1}$	$\Gamma_j (\gamma_j), \text{cm}^{-1}$	$\Delta\varepsilon_j$	$\omega_{0j} (\omega_{\text{pl},j}), \text{cm}^{-1}$	$\Gamma_j (\gamma_j), \text{cm}^{-1}$
300 K									
Drude ₁	—	4400	40	—	1960	156	—	2622	162
Drude ₂	—	22000	2960	—	17340	2650	—	14833	1717
Drude _{tot}	—	22500	—	—	17450	—	—	15060	—
Drude _{KK}	—	22000	—	—	17895	—	—	15300	—
L ₁	35	6121	9683	40	5407	9167	46	4888	8200
L ₂	14.25	18592	36627	13.8	19138	37238	12.7	18930	33539
L ₃	0.68	31035	16374	0.397	31325	17580	0.27	31483	20992
L ₄	2.35	58810	44568	2.47	58087	39548	2.57	53464	38045
L ₅	1.35	113407	3991	1.04	165782	3102	1	80467	3011
T_N									
Drude ₁	—	5900	40	—	2150	144	—	2300	600
Drude ₂	—	20475	2724	—	17315	2785	—	13212	1310
Drude _{tot}	—	21308	—	—	17448	—	—	13410	—
Drude _{KK}	—	20870	—	—	17915	—	—	13335	—
L ₁	33.7	6353	9503	37.3	5614	8928	45	4986	7956
L ₂	14.8	18096	35971	13.98	19138	37238	12.5	19460	34555
L ₃	0.7	30703	13062	0.39	31322	16222	0.2	32164	14191
L ₄	2.36	58461	44615	2.44	58087	38761	2.2	52906	33500
L ₅	1.64	273090	8172	0.92	138292	2947	1.12	70949	22284

doped $\text{Ba}_{1-x}\text{K}_x\text{Fe}_2\text{As}_2$ (see Ref. 63), shows a systematic softening with increasing atomic number of the intercalating atom, with a concomitant increase in $\Delta\varepsilon$. The evolution of the total zero-frequency interband permittivity $\Delta\varepsilon_{\text{tot}}$ is relatively small and is dominated by that of the lowest interband transition, as can be inferred from the limiting zero-frequency behavior of the total interband contribution to the real part of the dielectric function shown with black lines in Figs. 6(d)–6(f) and from Table II.

The extracted itinerant response (grey lines in Fig. 6) can be broken down into a narrow and broad component (see Table II) for all three compounds, in agreement with Ref. 16, which previously identified this phenomenon in essentially all known parent iron pnictides of the ThCr_2Si_2 type. In our Drude-Lorentz fit we excluded the lowest far-infrared spectral range strongly affected by the collective excitation in the Sr- and Ba-based compounds [gray shaded areas in Figs. 6(b), 6(c), 6(e), and 6(f)]. The two Drude contributions to the itinerant response are plotted in Fig. 6 as black dashed lines and their plasma frequencies and quasiparticle scattering rate are listed in Table II. The total plasma frequency of the free electrons $\omega_{\text{pl}}^{\text{tot}} = \sqrt{\omega_{\text{pl},1}^2 + \omega_{\text{pl},2}^2}$ shows a systematic increase with decreasing atomic number of the intercalant and is significantly larger in CaFe_2As_2 than in the other two compounds (see Fig. 6 and Table II). This trend is also weakly present in first-principles calculations of the plasma

frequency⁶⁴ but is significantly enhanced by renormalization in the real materials.

To further confirm the values of the total plasma frequency inferred from our Drude-Lorentz fit, we carried out a Kramers-Kronig consistency analysis of ellipsometric data. This analytical technique, utilizing the unique capacity of ellipsometry to independently obtain the real and imaginary part of the dielectric function,⁵¹ allows one to accurately determine the spectral weight contained in the extrapolation region at lowest frequencies and thus accurately measure the total plasma frequency of itinerant charge carriers. This is made possible by comparing the Kramers-Kronig transformation of the extrapolated real part of the optical conductivity with the independently obtained real part of the dielectric function, as shown in Fig. 5(e) and the inset therein. The total plasma frequencies for all three compounds obtained with this method are shown in Table II. It is clear that the agreement between $\omega_{\text{pl}}^{\text{tot}}$ obtained using the Drude-Lorentz fit and by means of a Kramers-Kronig consistency check is remarkable. It should be noted that the accuracy of the Kramers-Kronig consistency check in determining the total spectral weight and thus plasma frequency is extremely high (below 0.5% in the present case) and this approach only very weakly depends on the shape of extrapolation.⁵¹

The systematic enhancement of the itinerant response with decreasing atomic number of the intercalant, together with the results of the previous sections, shows that a number of

electronic properties are significantly enhanced in CaFe_2As_2 compared to its Sr- and Ba-based counterparts.

IV. CONCLUSIONS

In summary, we have reported a systematic comparison of the charge dynamics in three representative parent compounds of 122-type iron-based superconductors (CaFe_2As_2 , SrFe_2As_2 , and BaFe_2As_2) in a broad spectral range as well as a detailed temperature dependence of their far-infrared conductivity. We identified two spin-density-wave energy gaps in all three compounds, with a significantly stronger coupling in the Ca-based material within both spin-density-wave subsystems as compared to the other two compounds, in which the larger gap decreases systematically with increasing atomic number of the intercalant. Our detailed temperature measurements of the far-infrared conductivity of the three compounds allowed us to accurately track the temperature dependence of both spin-density-wave gaps and reveal an anomaly in CaFe_2As_2 in the energy range of the smaller gap at $T^* \approx 80$ K, well below the Néel temperature of this compound. The presence of this remnant transition implies that the two spin-density-wave subsystems are very weakly coupled to one another. A comparison to the temperature dependence of the far-infrared conductivity of SrFe_2As_2 and BaFe_2As_2 shows a clear evolution of this coupling from weak in the Ca-based compound via intermediate in the Sr-based to strong in the Ba-based material. The temperature dependence of the infrared phonons reveals a clear anomaly at T_N in all three compounds, whereby the spin-density-wave-induced modifications of the phonon properties set in exactly at T_N in both Ba- and Sr-based materials but at somewhat higher temperatures in CaFe_2As_2 , suggesting the early development of spin-density-wave fluctuations and their siz-

able impact on the lattice. The temperature dependence of the intensity $\Delta\varepsilon_0$ of the Ca-related phonon shows a possible signature of T^* . Similarly to the previously reported spin-density-wave-induced suppression of two absorption bands in SrFe_2As_2 , we find an analogous effect in both Ca- and Ba-based compounds, as well as a systematic evolution of the intensity of the suppression with the atomic number of the intercalant. The investigation of the spectral-weight transfer induced by the spin-density-wave transition reveals that in all three parent compounds energies much larger than the characteristic magnetic energy scales proposed for these materials are involved. This high-energy modification of the spectral weight might originate in a redistribution of the electronic population between several bands at the transition. Our accurate dispersion analysis of the independently obtained real and imaginary parts of the optical conductivity by means of spectroscopic ellipsometry reveals a strongly enhanced plasma frequency in CaFe_2As_2 , decreasing systematically with increasing atomic number of the intercalating atom. Our results single out CaFe_2As_2 in the class of ThCr_2Si_2 -type iron-based materials by demonstrating the existence of two weakly coupled but extremely metallic electronic subsystems. Since the three investigated materials are driven superconducting upon doping, our results may provide insights into the physics of the related superconductors.

V. ACKNOWLEDGEMENTS

This project was supported by the German Science Foundation under grant BO 3537/1-1 within SPP 1458. We gratefully acknowledge Y.-L. Mathis for support at the infrared beamline of the synchrotron facility ANKA at the Karlsruhe Institute of Technology and V. Khanna for taking part in some of the measurements.

-
- * Currently at: Leibniz Institute for Solid State and Materials Research, IFW, D-01069 Dresden, Germany
- ¹ Y. Kamihara, T. Watanabe, M. Hirano and H. Hosono, *J. Am. Chem. Soc.* **130**, 3296 (2008).
 - ² D. C. Johnston, *Adv. Phys.* **59**, 803 (2010).
 - ³ G. R. Stewart, *Rev. Mod. Phys.* **83**, 1589–1652 (2011).
 - ⁴ M. Rotter, M. Tegel, D. Johrendt, I. Schellenberg, W. Hermes and R. Pöttgen, *Phys. Rev. B* **78**, 020503 (2008).
 - ⁵ M. Rotter, M. Tegel and D. Johrendt, *Phys. Rev. Lett.* **101**, 107006 (2008).
 - ⁶ A. S. Sefat, R. Jin, M. A. McGuire, B. C. Sales, D. J. Singh and D. Mandrus, *Phys. Rev. Lett.* **101**, 117004 (2008).
 - ⁷ J.-H. Chu, J. G. Analytis, C. Kucharczyk and I. R. Fisher, *Phys. Rev. B* **79**, 014506 (2009).
 - ⁸ X. F. Wang, T. Wu, G. Wu, H. Chen, Y. L. Xie, J. J. Ying, Y. J. Yan, R. H. Liu and X. H. Chen, *Phys. Rev. Lett.* **102**, 117005 (2009).
 - ⁹ F. Hardy, P. Adelman, T. Wolf, H. Löhneysen and C. Meingast, *Phys. Rev. Lett.* **102**, 187004 (2009).
 - ¹⁰ M. Rotter, M. Pangerl, M. Tegel and D. Johrendt, *Angew. Chem. Int. Ed.* **47**, 7949–7952 (2008).
 - ¹¹ F. Rullier-Albenque, D. Colson, A. Forget, P. Thuéry and S. Poissonnet, *Phys. Rev. B* **81**, 224503 (2010).
 - ¹² A. Thaler, N. Ni, A. Kracher, J. Q. Yan, S. L. Bud'ko and P. C. Canfield, *Phys. Rev. B* **82**, 014534 (2010).
 - ¹³ S. Jiang, H. Xing, G. Xuan, C. Wang, Z. Ren, C. Feng, J. Dai, Z. Xu and G. Cao, *J. Phys.: Condens. Matter* **21**, 382203 (2009).
 - ¹⁴ D. N. Basov and A. V. Chubukov, *Nature Phys.* **7**, 272–276 (2011).
 - ¹⁵ W. Z. Hu, J. Dong, G. Li, Z. Li, P. Zheng, G. F. Chen, J. L. Luo and N. L. Wang, *Phys. Rev. Lett.* **101**, 257005 (2008).
 - ¹⁶ D. Wu, N. Barišić, P. Kallina, A. Faridian, B. Gorshunov, N. Drichko, L. J. Li, X. Lin, G. H. Cao, Z. A. Xu, N. L. Wang and M. Dressel, *Phys. Rev. B* **81**, 100512 (2010).
 - ¹⁷ M. Nakajima, S. Ishida, K. Kihou, Y. Tomioka, T. Ito, Y. Yoshida, C. H. Lee, H. Kito, A. Iyo, H. Eisaki, K. M. Kojima and S. Uchida, *Phys. Rev. B* **81**, 104528 (2010).
 - ¹⁸ H. Okamura, K. Shoji, M. Miyata, H. Sugawara, T. Moriwaki and Y. Ikemoto, arXiv:1303.4182 (unpublished) (2013).
 - ¹⁹ N. Ni, S. Nandi, A. Kreyssig, A. I. Goldman, E. D. Mun, S. L. Bud'ko and P. C. Canfield, *Phys. Rev. B* **78**, 014523 (2008).
 - ²⁰ L. Harnagea, S. Singh, G. Friemel, N. Leps, D. Bombor, M.

- Abdel-Hafiez, A. U. B. Wolter, C. Hess, R. Klingeler, G. Behr, S. Wurmehl and B. Büchner, *Phys. Rev. B* **83**, 094523 (2011).
- ²¹ S. Ran, S. L. Bud'ko, W. E. Straszheim, J. Soh, M. G. Kim, A. Kreyssig, A. I. Goldman and P. C. Canfield, *Phys. Rev. B* **85**, 224528 (2012).
- ²² T.-M. Chuang, M. P. Allan, J. Lee, Y. Xie, N. Ni, S. L. Budko, G. S. Boebinger, P. C. Canfield and J. C. Davis, *Science* **327**, 181 (2010).
- ²³ M. P. Allan, T.-M. Chuang, F. Masee, Y. Xie, N. Ni, S. L. Budko, G. S. Boebinger, Q. Wang, D. S. Dessau, P. C. Canfield, M. S. Golden and J. C. Davis, *Nature* **9**, 220–224 (2013).
- ²⁴ J.-H. Chu, J. G. Analytis, K. De Greve, P. L. McMahon, Z. Islam, Y. Yamamoto and I. R. Fisher, *Science* **329**, 824–826 (2010).
- ²⁵ J.-H. Chu, H.-H. Kuo, J. G. Analytis and I. R. Fisher, *Science* **337**, 710–712 (2012).
- ²⁶ S. Ishida, M. Nakajima, T. Liang, K. Kihou, C. H. Lee, A. Iyo, H. Eisaki, T. Kakeshita, Y. Tomioka, T. Ito and S. Uchida, *Phys. Rev. Lett.* **110**, 207001 (2013).
- ²⁷ M. Nakajima, S. Ishida, Y. Tomioka, K. Kihou, C. H. Lee, A. Iyo, T. Ito, T. Kakeshita, H. Eisaki and S. Uchida, *Phys. Rev. Lett.* **109**, 217003 (2012).
- ²⁸ M. Nakajima, S. Ishida, K. Kihou, Y. Tomioka, T. Ito, C. Lee, H. Kito, A. Iyo, H. Eisaki, K. Kojima and S. Uchida, *Phys. C: Supercond.* **470**, S326–S327 (2010).
- ²⁹ W. Z. Hu, Q. M. Zhang and N. L. Wang, *Phys. C: Supercond.* **469**, 545–558 (2009).
- ³⁰ D. Wu *et al.*, *Phys. Rev. B* **79**, 155103 (2009).
- ³¹ A. A. Schafgans, B. C. Pursley, A. D. LaForge, A. S. Sefat, D. Mandrus and D. N. Basov, *Phys. Rev. B* **84**, 052501 (2011).
- ³² B. Cheng, B. F. Hu, R. Y. Chen, G. Xu, P. Zheng, J. L. Luo and N. L. Wang, *Phys. Rev. B* **86**, 134503 (2012).
- ³³ G. Li, W. Z. Hu, J. Dong, Z. Li, P. Zheng, G. F. Chen, J. L. Luo and N. L. Wang, *Phys. Rev. Lett.* **101**, 107004 (2008).
- ³⁴ B. Gorshunov, D. Wu, A. A. Voronkov, P. Kallina, K. Iida, S. Haindl, F. Kurth, L. Schultz, B. Holzapfel and M. Dressel, *Phys. Rev. B* **81**, 060509 (2010).
- ³⁵ T. Fischer, A. V. Pronin, J. Wosnitza, K. Iida, F. Kurth, S. Haindl, L. Schultz, B. Holzapfel and E. Schachinger, *Phys. Rev. B* **82**, 224507 (2010).
- ³⁶ A. Lucarelli, A. Dusza, F. Pfuner, P. Lerch, J. G. Analytis, J.-H. Chu, I. R. Fisher and L. Degiorgi, *New J. Phys.* **12**, 073036 (2010).
- ³⁷ D. Wu, N. Barišić, M. Dressel, G. H. Cao, Z. A. Xu, J. P. Carbotte and E. Schachinger, *Phys. Rev. B* **82**, 184527 (2010).
- ³⁸ J. J. Tu, J. Li, W. Liu, A. Punnoose, Y. Gong, Y. H. Ren, L. J. Li, G. H. Cao, Z. A. Xu and C. C. Homes, *Phys. Rev. B* **82**, 174509 (2010).
- ³⁹ N. Barišić, D. Wu, M. Dressel, L. J. Li, G. H. Cao and Z. A. Xu, *Phys. Rev. B* **82**, 054518 (2010).
- ⁴⁰ A. A. Schafgans, S. J. Moon, B. C. Pursley, A. D. LaForge, M. M. Qazilbash, A. S. Sefat, D. Mandrus, K. Haule, G. Kotliar and D. N. Basov, *Phys. Rev. Lett.* **108**, 147002 (2012).
- ⁴¹ D. Wu, G. Chanda, H. S. Jeevan, P. Gegenwart and M. Dressel, *Phys. Rev. B* **83**, 100503 (2011).
- ⁴² S. J. Moon *et al.*, *Phys. Rev. Lett.* **109**, 027006 (2012).
- ⁴³ M. Nakajima, T. Tanaka, S. Ishida, K. Kihou, C. H. Lee, A. Iyo, T. Kakeshita, H. Eisaki and S. Uchida, *Phys. Rev. B* **88**, 094501 (2013).
- ⁴⁴ M. Nakajima *et al.*, arXiv:1308.6113 (unpublished) (2013).
- ⁴⁵ M. Nakajima *et al.*, arXiv:1308.6133 (unpublished) (2013).
- ⁴⁶ E. J. Nicol and J. P. Carbotte, *Phys. Rev. B* **71**, 054501 (2005).
- ⁴⁷ V. G. Kogan, C. Martin and R. Prozorov, *Phys. Rev. B* **80**, 014507 (2009).
- ⁴⁸ Y. Ponomarev, S. Kuzmichev, M. Mikheev, M. Sudakova, S. Tchesnokov, T. Shanygina, O. Volkova, A. Vasiliev and T. Wolf, *J. Exp. Theor. Phys.* **113**, 459–467 (2011).
- ⁴⁹ R. Khasanov, M. Bendele, A. Amato, K. Conder, H. Keller, H.-H. Klauss, H. Luetkens and E. Pomjakushina, *Phys. Rev. Lett.* **104**, 087004 (2010).
- ⁵⁰ Y. Ponomarev *et al.*, *J. Supercond. Nov. Magn.* **26**, 2867–2871 (2013).
- ⁵¹ A. Charnukha, P. Popovich, Y. Matiks, D. L. Sun, C. T. Lin, A. N. Yaresko, B. Keimer and A. V. Boris, *Nature Commun.* **2**, 219 (2011).
- ⁵² G. L. Sun, D. L. Sun, M. Konuma, P. Popovich, A. Boris, J. B. Peng, K.-Y. Choi, P. Lemmens and C. T. Lin, *J. Supercond. Nov. Magn.* **24**, 1773 (2011).
- ⁵³ A. V. Boris, N. N. Kovaleva, S. S. A. Seo, J. S. Kim, P. Popovich, Y. Matiks, R. K. Kremer and B. Keimer, *Phys. Rev. Lett.* **102**, 027001 (2009).
- ⁵⁴ R. Kubo, *J. Phys. Soc. Jap.* **12**, 570–586 (1957).
- ⁵⁵ O. V. Dolgov and M. L. Kulić, *Phys. Rev. B* **66**, 134510 (2002).
- ⁵⁶ C. Bernhard, T. Holden, A. V. Boris, N. N. Kovaleva, A. V. Pimenov, J. Humlicek, C. Ulrich, C. T. Lin and J. L. Tallon, *Phys. Rev. B* **69**, 052502 (2004).
- ⁵⁷ D. N. Basov, A. V. Puchkov, R. A. Hughes, T. Strach, J. Preston, T. Timusk, D. A. Bonn, R. Liang and W. N. Hardy, *Phys. Rev. B* **49**, 12165–12169 (1994).
- ⁵⁸ R. P. S. M. Lobo, Y. M. Dai, U. Nagel, T. Rößler, J. P. Carbotte, T. Timusk, A. Forget and D. Colson, *Phys. Rev. B* **82**, 100506 (2010).
- ⁵⁹ H. K. Ng, M. Capizzi, G. A. Thomas, R. N. Bhatt and A. C. Gosard, *Phys. Rev. B* **33**, 7329–7331 (1986).
- ⁶⁰ A. Gold, S. J. Allen, B. A. Wilson and D. C. Tsui, *Phys. Rev. B* **25**, 3519–3528 (1982).
- ⁶¹ H. F. Jang, G. Cripps and T. Timusk, *Phys. Rev. B* **41**, 5152–5168 (1990).
- ⁶² R. Mittal *et al.*, *Phys. Rev. B* **79**, 144516 (2009).
- ⁶³ A. Charnukha, O. V. Dolgov, A. A. Golubov, Y. Matiks, D. L. Sun, C. T. Lin, B. Keimer and A. V. Boris, *Phys. Rev. B* **84**, 174511 (2011).
- ⁶⁴ S.-L. Drechsler, F. Roth, M. Grobosch, R. Schuster, K. Koepf, H. Rosner, G. Behr, M. Rotter, D. Johrendt, B. Büchner and M. Knupfer, *Phys. C: Supercond.* **470**, S332–S333 (2010).
- ⁶⁵ To facilitate the comparison with previous work, in this section we use electron-volt instead of wavenumber as the unit of photon energy. The conversion factor between the two is $8066\text{ cm}^{-1}/\text{eV}$.